Article

Synthesis of a Ru(II) Complex with a Naphthoquinone-Annelated Imidazole Ligand Exhibiting Proton-Responsive Redox and Luminescent Behavior

Takuya Shiga [1,*] **, Minami Tachibana** [1] **, Hiroki Oshio** [1,2] **and Masayuki Nihei** [1]

[1] Graduate School of Pure and Applied Sciences, University of Tsukuba, Tennodai 1-1-1, Tsukuba, Ibaraki 305-8571, Japan; jam.mm1802@gmail.com (M.T.); oshio@chem.tsukuba.ac.jp (H.O.); nihei@chem.tsukuba.ac.jp (M.N.)

[2] State Key Laboratory of Fine Chemicals, Dalian University of Technology, 2 Linggong Rd., Dalian 116024, China

* Correspondence: shiga@chem.tsukuba.ac.jp; Tel.: +81-29-853-4426

Abstract: A mononuclear ruthenium complex, $[Ru^{II}(L)(bpy)_2](PF_6)$, with a naphthoquinone-annelated imidazole ligand HL (2-(pyridin-2-yl)-1H-naphtho[2,3-d]imidazole-4,9-dione) was synthesized and structurally characterized. Electrochemical study reveals that the Ru complex shows four reversible redox waves at +0.98 V, −1.13 V, −1.53 V, and −1.71 V versus SCE in acetonitrile, which are assigned to Ru(II)/Ru(III), $L^-/L^{\bullet 2-}$, and two bpy/bpy$^{\bullet-}$ redox couples, respectively. The redox potential of Ru(II)/Ru(III) was positively shifted upon the addition of trifluoromethanesulfonic acid due to protonation of the L^- moiety, leading to stabilization of the Ru 4d orbital. In UV-vis absorption measurements for the Ru complex in acetonitrile, a metal-to-ligand charge transfer (MLCT) band was observed at 476 nm, which was shifted to 450 nm by protonation, which might be due to a decrease in the electron delocalization and stabilization of the π orbitals in L^-. The blue shift of the MLCT band by protonation was associated with a shift of an emission band from 774 nm to 620 nm, which could be caused by the decreased electronic delocalization in the MLCT excited state. These electrochemical and spectroscopic changes were reversible for the protonation/deprotonation stimuli.

Keywords: Ru(II) complex; single-crystal X-ray crystallography; electrochemistry; luminescence

1. Introduction

Stimuli-responsive materials have attracted considerable attention for their potential application as smart materials in the field of optoelectronics and life science [1–3]. Various external stimuli, such as temperature, pressure, and light, have been utilized to control the physical properties of metal complexes [4,5]. In addition, chemical stimuli, such as guest molecules/ions, humidity, and protons, have been employed as a trigger of the electronic and structural changes [6–10]. Among them, the proton is one of the easy-to-use triggers, inducing physical property changes, and many proton-responsive compounds have been intensively studied. pH-responsive luminescence materials have been widely investigated from the viewpoint of environmental and life science [11,12]. On the other hand, protons play an important role in biological systems, in which redox behavior is significantly altered through the proton-coupled electron transfer (PCET) process [13,14], and the pH-dependent redox reactions of ruthenium complexes have been intensively studied to understand the interplay between electrons and protons [15–18]. In the field of solid state chemistry, proton dynamics and modulation of hydrogen bonds have been extensively studied in various types of switching materials [19–22], and many interesting physical properties, such as protonation-affected spin transition behavior in metal complexes [23–26], solid state proton transfer induced by spin-crossover phenomena [27], and proton dynamics-directed phase transition in conducting organic molecules [28].

We have previously reported Fe(II) complexes with a naphthoquinone-annelated imidazolate ligand L⁻ (HL = 2-(pyridin-2-yl)-1*H*-naphtho[2,3-*d*]imidazole-4,9-dione), [Fe^{II}(L)$_2$(L$^{1-4}$)$_2$] (L^1 = ethylenediamine, L^2 = cyclohexanediamine, L^3 = diamino benzoquinone, L^4 = iminosuccinonitrile), and their spin-crossover behavior in solid state was reported [29]. The naphthoquinone moiety in HL is expected to show a proton response and redox activities and to be a good building block for the proton-responsive coordination complex. On the other hand, ruthenium complexes have been afforded a family of luminescent and redox-active systems originating from their high thermal stability and strong spin-orbit coupling [30–33]. Various functional ligands, such as 1,10-phenanthroline, 2,9-di(pyrid-2′-yl)-1,10-phenanthroline, 2,6-di(quinoline-8-yl)pyridine, and 2-(2′-pyridyl)naphthoimidazole, have been employed to modify the molar absorptivity, emission energy, and excited-state lifetime of the Ru complexes [34–38]. From the viewpoints described above, exploration of the functional ligands for Ru complexes is important. The naphthoquinone-annelated multidentate ligand could show various electronic states by protonation and redox process and be useful for switching the functions of the Ru complexes. We report here a mononuclear ruthenium complex, [Ru^{II}(L)(bpy)$_2$](PF$_6$) (**1**), with naphthoquinone-annelated imidazole ligand L⁻ (HL = 2-(pyridin-2-yl)-1*H*-naphtho[2,3-d]imidazole-4,9-dione), exhibiting proton-responsive redox and emission properties.

2. Results and Discussion

2.1. Structure of [Ru(L)(bpy)$_2$](PF$_6$)·AcOEt·0.5MeOH (1)

Single crystals of complex **1** suitable for X-ray diffraction measurements were obtained by recrystallization of **1** in MeOH/EtOAc. Complex **1** crystallized in the monoclinic space group $P2_1/c$ and consists of one complex cation, [Ru(L)(bpy)$_2$]$^+$, and one PF$_6$⁻ anion. In the crystal lattice, there is one AcOEt molecule and half of an MeOH molecule per one complex cation (Figure 1, Table 1). In [Ru(L)(bpy)$_2$]$^+$, deprotonated naphthoquinone-annelated imidazolate, L⁻, acts as a mono-anionic bidentate ligand and coordinates with the ruthenium ion. The ruthenium ion has an octahedral coordination geometry with N$_6$ donor atoms, of which the four are bipyridine nitrogen atoms and the two are nitrogen atoms of pyridine and imidazolate moieties donated by the L⁻ ligand. Thus, the coordination environment can be regarded as five pyridines and one imidazolate functionality. The two C–N bond distances of the imidazolate moiety (C6-N2: 1.374 Å, C6-N3: 1.327 Å) suggests that the deprotonated imidazolate group coordinates to ruthenium ion. By considering the above structural features, **1** is a ruthenium complex containing a Ru(II) ion with a chemical formula of [Ru(L)(bpy)$_2$](PF$_6$)·AcOEt·0.5MeOH. The ligand reveals a novel binding behavior of the imidazole entity. So far, the coordination of an imine nitrogen was observed, exemplarily found in the respective naphthyl analogue complex [Ru(II)(bpy)$_2$(PYNI)](ClO$_4$)$_2$ (PYNI = 2-(2′-pyridyl)naphthoimidazole)) [37]. Instead, complex **1** has an imidazolate coordination site, formed upon deprotonation. This fact was confirmed by IR data, in which there is no N–H stretch band of the imidazole group.

2.2. Electrochemistry

The electrochemical properties of HL and complex **1** were investigated by cyclic voltammetry (CV). The resultant cyclic voltammograms are shown in Figure 2, and the redox potentials ($E_{1/2}$) and their assignments are provided in Table 2. HL shows two reversible redox waves at $E_{1/2}$ = −0.63 and −1.30 V versus SCE, which are assigned to the two-step reduction in naphthoquinone moieties through a formation of a semiquinone radical anion as an intermediate [39]. Complex **1** shows one oxidation wave at +0.98 V, and three reduction waves at −1.13 V, −1.53 V, and −1.71 V. The reversible oxidation wave corresponds to a Ru(II)/Ru(III) redox couple characteristic of Ru(II) complexes with diimine ligands [40]. It is well known that the Ru(II) complex with two bpy ligands, [Ru(bpy)$_2$(L′)] (L′ = polypyridine-type ligands), exhibit two successive reduction process at ca. −1.4 and ca. −1.8 V due to the stepwise reduction of two bpy ligands [40–44]. The redox potentials of the second and third reduction waves in **1** are comparative to the reported reduction
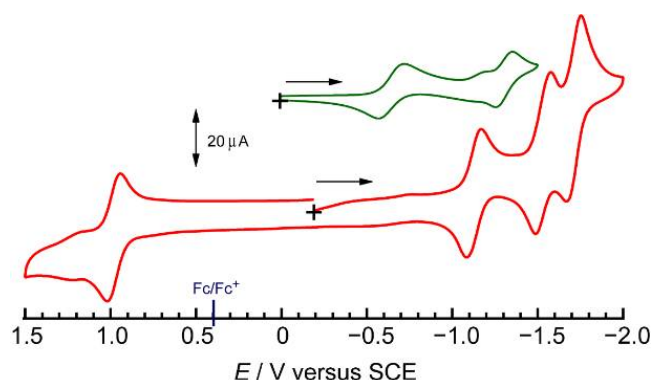
potentials in [Ru(bpy)$_2$(L′)]; therefore, they can be assigned to the two bpy/bpy$^{\bullet-}$ redox couples. Considering the redox potential of bpy in the [Ru(bpy)$_3$]$^{2+}$ complex (-1.36, -1.52, -1.76 V vs. SCE), the second and third reduction waves for complex **1** correspond to a two-step reduction of bpy/bpy$^{\bullet-}$. The first reduction wave at -1.13 V is assignable to a reduction of the naphthoquinone moiety in L$^-$ by considering the redox behavior of HL. Note that HL shows two large reduction peaks at -0.63 and -1.30 V and one small peak at -1.1 V. The main two reduction peaks can be assigned as HL/L$^{\bullet-}$ and HL$^{\bullet-}$/HL^{2-}, while the small peak was originated from the existence of a dimer of the neutral-anion radical complex [45]. The first redox potential of the naphthoquinone moiety in **1** was negatively shifted compared with that in the protonated HL, which could be due to the deprotonation of the imidazole moiety in **1**. Consequently, the three-step reduction process in **1** is originating from the reversible reduction reactions of L$^-$/L$^{\bullet2-}$, and two bpy/bpy$^{\bullet-}$, respectively. These redox potentials of Ru(II)/Ru(III) and two bpy ligands are close to the values of the redox potentials for the naphthyl analogs [Ru(II)(bpy)$_2$(PYNI)](ClO$_4$)$_2$ (Ru(II)/Ru(III) 1,16 V vs. SCE; bpy/bpy$^{\bullet-}$ -1.44 and -1.68 V vs. SCE) [37].

(a) (b)
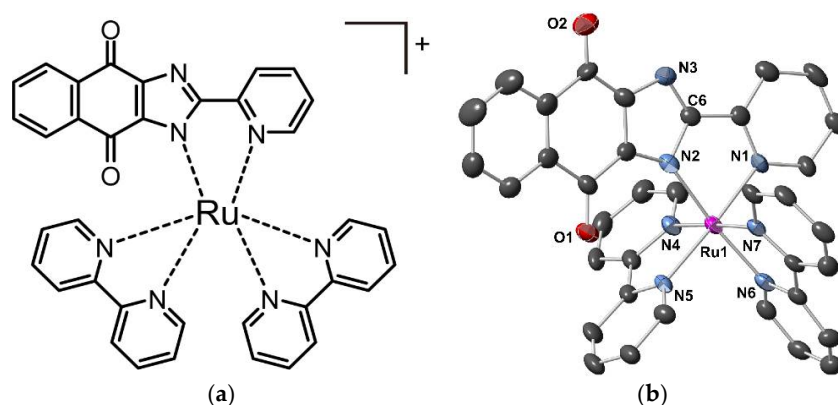
Figure 1. (**a**) A chemical structure of the complex cation in **1**. The PF$_6^-$ counter ion is omitted. (**b**) An ORTEP representation of the complex cation in **1**. All H atoms and solvent molecules were removed for clarity. Selected bond lengths: Ru–N1 2.076(5), Ru–N2 2.079(6), Ru–N4 2.044(6), Ru–N5 2.049(5), Ru–N6 2.047(6), and Ru–N7 2.050(5) Å.

Table 1. X-ray crystallographic data for complex **1**.

Compound	[Ru(L)(bpy)$_2$](PF$_6$)·AcOEt·0.5MeOH
Formula	C$_{40.5}$H$_{35}$F$_6$N$_7$O$_{4.5}$PRu
M/g mol^{-1}	937.79
Crystal system	Monoclinic
Space group	$P2_1$/c
a/Å	8.431(3)
b/Å	35.524(14)
c/Å	13.404(5)
β/deg.	99.315(4)
Volume/Å^3	3962(3)
Z	4
T/K	100(2)
ρ_{calc}/g cm^{-3}	1.571
μ mm^{-1}	0.518
Data/Parameters	9017/553
R_{int}	0.0999
GOF	1.032
R_1 (>2$\sigma(I)$)	0.0773
wR_2 (>2$\sigma(I)$)	0.1962

Figure 2. Cyclic voltammograms of HL (green) and complex **1** (red) in acetonitrile. Open circuit potentials and the initial scan directions are indicated by the black cross and arrow.

Table 2. Redox potentials for complex **1**, HL, and $[Ru(bpy)_3]^{2+}$ (versus SCE). The difference between $E_{p,c}$ (peak potential of cathodic current) and $E_{p,a}$ (peak potential of anodic current) is shown in parenthesis.

$E_{1/2}$/V	Ru(II)/Ru(III)		$L^-/L^{\bullet 2-}$	bpy/bpy$^{\bullet-}$	bpy/bpy$^{\bullet-}$	bpy/bpy$^{\bullet-}$
1	+0.98 (0.08)		−1.13 (0.08)		−1.53 (0.09)	−1.71 (0.08)
		HL/HL$^{\bullet-}$				
HL		−0.63 (0.16)				
	Ru(II)/Ru(III)			bpy/bpy$^{\bullet-}$	bpy/bpy$^{\bullet-}$	bpy/bpy$^{\bullet-}$
$[Ru(bpy)_3]^{2+}$	+ 1.25			−1.36	−1.52	−1.76

Solvent: MeCN; electrolyte: TBAPF$_6$.

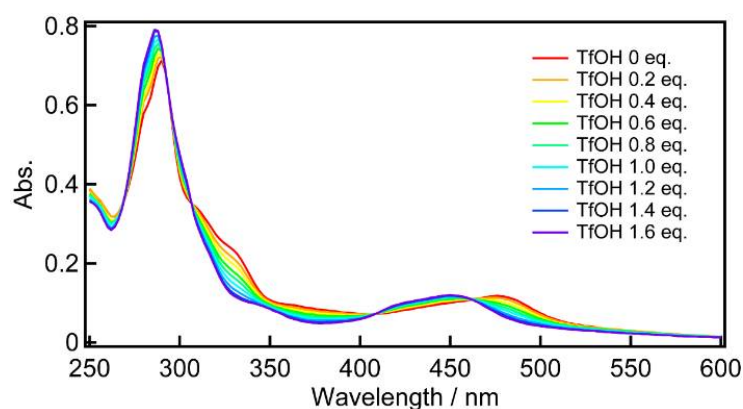## 2.3. UV-Vis and Emission Spectra

Absorption spectra of complex **1** in acetonitrile are shown in Figure 3a. The most intense absorption bands were observed around 300 nm, with the shoulders in the range of 300–350 nm, while two characteristic bands were observed at 444 and 476 nm. $[Ru^{II}(bpy)_3]^{2+}$ is reported to show a π–π^* transition band at 285 nm and a $Ru(d\pi) \rightarrow bpy(\pi^*)$ metal-to-ligand charge transfer (MLCT) band at 458 nm [35]. By considering the band assignments in $[Ru(bpy)_3]^{2+}$ and relating complexes [35], the most intense absorption bands around 300 nm in **1** originate from the π–π^* transition bands in two bpy moieties, while lower energy absorption bands at 300–350 nm are assignable to the π–π^* transition bands in the L^- moiety. HL and L^- showed π–π^* transition bands at 382 nm and 450 nm, respectively, which are lower in energy than that in bpy. These data supported the assignments mentioned above. These assignments were supported by the electrochemical data in Section 2.2. The reduction potential of L^- is more positive than that of bpy, indicating the lower-lying π^* orbitals in L^-, which may be due to the extended π conjugated structure of L^- and cause the lower π–π^* excitation energy in the L^- moiety. The two absorption bands at 444 and 476 nm can be assigned to $Ru(d\pi) \rightarrow bpy(\pi^*)$ and $Ru(d\pi) \rightarrow L^-(\pi^*)$ MLCT because the stabilized π^* bands in L^- should cause the lower energy MLCT band than that in bpy. This assignment is supported by the TD-DFT calculation on **1** (Figure S4, Table S1). The calculated transition bands at 434 nm and 428 nm are assigned to MLCT Ru/bpy. On the other hand, the transition bands at 529 nm and 526 nm have a contribution of MLCT Ru/L$^-$. These lower energy transition bands appeared in the observed UV spectra. Emission spectra of **1** in acetonitrile were recorded and displayed in Figure 3b. Excitation of the MLCT bands gives rise to a broad emission band at 774 nm, which could be due to luminescence from the ^{3}MLCT excited state originating from the lowest energy $Ru(d\pi) \rightarrow L^-(\pi^*)$ excited state [35,37]. The relatively large Stokes shift (3.36×10^4 cm^{-1}, 298 nm) in **1** may be due to the charge delocalization on the naphthoquinone-annelated imidazole moiety in the excited state.
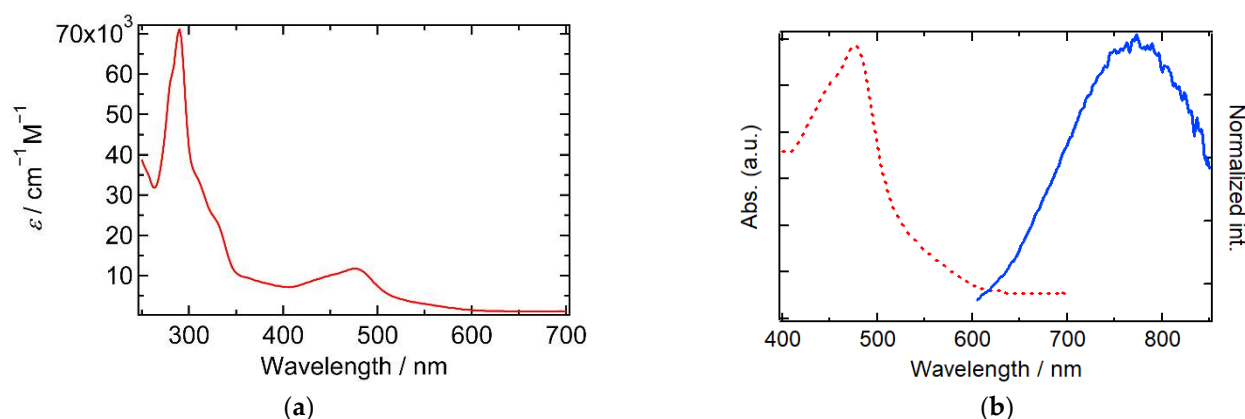
Figure 3. (**a**) UV-Vis absorption spectrum of complex **1** in acetonitrile ($c = 1.0 \times 10^{-5}$ M); (**b**) absorption (red dotted line) and emission (blue solid line) spectra of complex **1** in acetonitrile.

### 2.4. Effects of Protonation on the Electronic Structure

UV-vis absorption spectra were measured upon the addition of trifluoromethanesulfonic acid (TfOH) to a solution of **1** in MeCN, and the spectral change is shown in Figure 4. It should be noted that the spectral change showed isosbestic points at 307, 408, and 462 nm, which were not changed when increasing the amount of TfOH up to 1.6 eq. This result suggested that the spectral change is caused by a one-step protonation of the L^- moiety to yield a singly protonated **1** (H^+-**1**). With increasing the amount of TfOH, the π-π*(L^-) and $Ru(d\pi) \rightarrow L^-(\pi^*)$ MLCT absorption bands (290 nm and 478 nm) were shifted to higher energy region (286 nm and 450 nm), due to the protonation of the L^- moiety in H^+-**1**. The protonation may cause a decrease in electron delocalization due to a decrease in the resonance structures and stabilization of the π orbitals in L^-, leading to a higher excitation energy in the π-π* and $Ru(d\pi) \rightarrow L^-(\pi^*)$ MLCT transitions. The results of the TD-DFT calculations for the geometry-optimized H^+-**1** support the shift of the transition bands (Figure S5, Table S2). The electronic structure change of **1** upon protonation was proved by emission spectroscopy measurements.

Figure 4. UV-Vis absorption spectral changes of complex **1** with TfOH.

The ^{3}MLCT emission band at 774 nm was shifted to 620 nm upon addition of TfOH (Figure 5a), corresponding to the blue shift of the MLCT absorption bands by protonation of L^-. It should be noted that the protonated state shows a smaller Stokes shift of 5.88×10^4 cm^{-1} (170 nm), which could be caused by the decreased electronic delocalization in the L^- moiety of H^+-**1**. The emission band of H^+-**1** is close to that of $[Ru(bpy)_3]^{2+}$, suggesting emission from MLCT Ru/bpy. The spectroscopic changes due to protonation and deprotonation were reversible upon additions of TfOH and Et$_3$N (Figure S6, Supple-

mentary Materials). In CV, the redox wave of Ru(II)/Ru(III) couple was positively-shifted from +0.98 V to +1.23 V by the addition of 1.6 eq. of TfOH (Figure 5b). The stabilization of the Ru 4d orbital is ascribed to the electron-withdrawing effects from the protonated L^- moiety in $H^+-\mathbf{1}$. CV data of $H^+-\mathbf{1}$ in the potential range of $-2.0 - +1.5$ V is shown in Figure S7 (Supplementary Materials), in which $H^+-\mathbf{1}$ showed a complicated reduction processes due to adsorption of the reduced $H^+-\mathbf{1}$ on the electrode surface. Related works on pH-sensitive ruthenium(II) complexes $[Ru(bpy)_2L^{im}]^{n+}$ bearing imidazole-type ligands L^{im} have been reported [39,40]. In these works, the emission intensity decrease, and a slight red shift is observed with increasing the pH value. In the present work, a similar responsivity was observed; however, detailed understandings require the isolation of $H^+-\mathbf{1}$ and theoretical calculations.
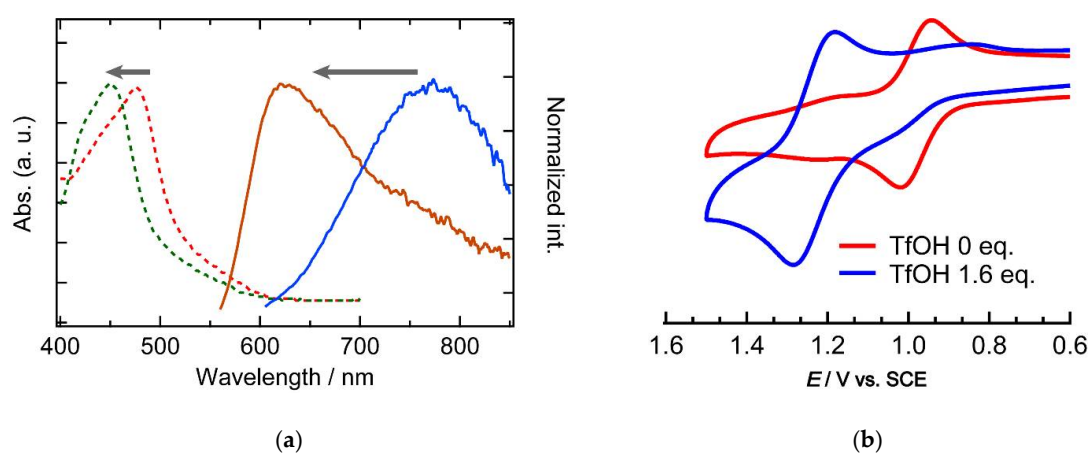
Figure 5. (**a**) Absorption and emission spectra and (**b**) cyclic voltammograms of complex **1** in acetonitrile before and after the addition of 1.6 eq. of TfOH.

3. Materials and Methods

3.1. Materials

All solvents and chemicals were reagent grade, purchased commercially, and used without further purification unless otherwise noted. The naphthoquinone-annelated ligand, 2-(pyridin-2-yl)-1*H*-naphtho[2,3-*d*]imidazole-4,9-dione (HL), was prepared by condensation of 2-pyridylcarboxaldehyde with 2,3-diaminonaphthoquinone, and $[RuCl_2(bpy)_2]$ was synthesized according to a previously reported procedure [41,46–48].

3.2. Microwave Reaction

Reactions were performed using a CEM Discover microwave unit. Reactions were performed in 10 mL capacity sealed tubes. The contents of the reaction vessel were stirred using an electromagnet located below the floor of the microwave cavity and a Teflon-coated magnetic stir bar in the vessel.

3.3. Synthesis of [Ru(L)(bpy)$_2$](PF$_6$)·2H$_2$O (1·2H$_2$O).

$[Ru(L)(bpy)_2](PF_6)\cdot2H_2O$ (**1**·$2H_2O$) was prepared by microwave-assisted synthesis. $[RuCl_2(bpy)_2]$ (34.69 mg, 0.067 mmol) and HL (18.35 mg, 0.067 mmol) were dissolved in ethylene glycol (5 mL) under nitrogen, and the mixture was irradiated by microwave for 15 min at 210 °C (200 W). The cooled reaction mixture was diluted with water (16.7 mL), followed by filtration to remove the insoluble precipitate to obtain a dark-red solution. The addition of an excess amount of $NaPF_6$ to the filtrate resulted in a reddish-brown suspension. The reddish-brown powder of the crude product was collected and washed with water (47.8 mg, yield: 86%). The obtained reddish-brown powder was dissolved in MeOH. The solution was filtered, and the filtrate was carefully layered with AcOEt. After several days, X-ray quality red needle crystals of $[Ru(L)(bpy)_2](PF_6)\cdot AcOEt\cdot0.5MeOH$ (**1**·AcOEt·0.5MeOH)

were collected by filtration, and dried in the air, affording [Ru(L)(bpy)$_2$](PF$_6$)·2H$_2$O (**1**·2H$_2$O). The collected crystals were used for all physical measurements. Yield: 24 mg (41%). MALDI-TOF-MS (m/z) [M]$^+$ calcd.: 688.10; found: 688.07, [M + H]$^{2+}$ calcd.: 344.55; found: 344.53. Anal. Calc. for C$_{36}$H$_{28}$F$_6$N$_7$O$_4$PRu ([Ru(L)(bpy)$_2$](PF$_6$)·2H$_2$O): C, 49.78; H, 3.25; N, 11.29%: Found: C, 50.11; H, 2.98; N, 11.13%. ^{1}H NMR (400 MHz, CD$_3$CN): δ 8.47−8.40(m, 5H), 8.06−7.95(m, 7H), 7.82(d, 1H), 7.74−7.63(m, 5H), 7.52(d, 1H), 7.38−7.25(m, 5H). ^{13}C{^{1}H} NMR (400 MHz, CD$_3$CN): δ 178.49, 177.92, 159.39, 159.36, 158.98, 158.54, 154.03, 153.65, 153.42, 153.25, 152.95, 152.74, 145.70, 144.91, 138.97, 138.63, 138.55, 138.35, 137.91, 135.37, 135.06, 134.71, 134.56, 128.93, 128.79, 128.30, 127.80, 127.61, 127.47, 125.54, 125.32, 124.70, 124.55. IR (KBr, cm^{-1}): 1659(s, $\nu_{C=O}$), 1593(m), 1466(s), 1447(s), 1221(s), 843(s, ν_{PF6^-}).

3.4. X-ray Crystallography

Crystals were mounted on a micromount, and the data were collected at −173 °C (Bruker SMART APEXII diffractometer coupled with a CCD area detector with graphite monochromated Mo*K*α (λ = 0.71073 Å radiation). The structure was solved using direct methods and expanded using Fourier techniques within the SHELXTL program [49]. Empirical absorption corrections were calculated using SADABS [50]. In the structure analyses, non-hydrogen atoms were refined with anisotropic thermal parameters. Hydrogen atoms were included in the calculated positions and refined with the isotropic thermal parameters riding on those of the parent atoms. Further crystallographic details can be found in the corresponding CIF file provided in the ESI. Crystallographic data for the structure reported in this work were deposited at the Cambridge Crystallographic Data Centre (CCDC) as supplementary publication number: CCDC-2058847. Copies of the data can be obtained online using https://summary.ccdc.cam.ac.uk/structure-summary-form (accessed on 30 January 2021).

3.5. Physical Measurements

Elemental analyses were performed using a Perkin-Elmer 2400 II CHN for the C, H, and N elements. Infrared absorption spectra were measured on KBr pellet samples using a SHIMADZU IRAffinity-1 spectrometer. UV-vis absorption spectra of MeCN solution in quartz cell with a path length of 1 cm were recorded on a SHIMADZU UV-3150 spectrometer. Fluorescence spectra were measured by a JASCO FP-8500 spectrofluorometer at room temperature. Measurements were performed using a degassed solvent. MALDI-TOF-MS measurements were performed using a time of flight (TOF) mass spectrometer (AB SCIEX TOF/TOF 5800 system) equipped with a matrix-assisted laser/desorption ionization (MALDI) source.

Titration experiments were performed as follows. A solution of **1** in MeCN was titrated by TfOH, and the spectra of the solution were recorded every 0.2 eq. of TfOH added.

3.6. Cyclic Voltammetry

Cyclic voltammetry measurements were carried out in a standard one compartment cell under N$_2$ at 20 °C equipped with a platinum wire counter electrode, a saturated calomel electrode (SCE) as the reference electrode, and a glassy carbon (GC) working electrode using an ALS BAS 620A electrochemical analyzer. The measurements were performed in acetonitrile with 0.1 M tetra-*n*-butylammonium hexafluorophosphate (N^{n}Bu$_4$PF$_6$) as the supporting electrolyte. The concentration of the complex **1** was 1 mM. The scan rate was 100 mV/sec.

3.7. DFT Calculations

DFT calculations were carried out using the B3LYP exchange correlation function and implemented in the *Gaussian 16* program package [51,52]. The electronic structures of the complexes were determined using a general basis set with the Los Alamos effective core potential LanL2DZ basis set [53–55]. Low-lying excitation energies were calculated with time-dependent DFT (TD-DFT). The conductor polarizable continuum model (CPCM)

was used to account for solvent effects on the electronic transitions [56]. The Cartesian coordinates of the geometry-optimized **1** and H+−**1** are shown in Tables S3 and S4.

4. Conclusions

We have synthesized a mononuclear ruthenium complex **1** with a naphthoquinone-annelated imidazole ligand HL. The single-crystal X-ray structure analysis revealed that **1** consists of a central Ru ion, a redox-active naphthoquinone moiety, and a proton-sensitive imidazolate moiety. In the electrochemical study, **1** showed a reversible one-step Ru(II)/Ru(III) oxidation and a three-step reduction containing a reversible reduction of the naphthoquinone moiety. In addition, a characteristic broad emission from an excited state is generated by the Ru(II) to L^- charge transfer. Consequently, **1** was proven to exhibit a characteristic redox and emission behavior based on the naphthoquinone moiety as an electron acceptor. Modulations of the redox and emission behavior were investigated by protonation. As a result, we found a significant change in the electronic structure of **1** by adding 1.6 eq. of TfOH, which is caused by the decrease in electronic delocalization in the L^- moiety by protonation. These results demonstrated that the naphthoquinone-annelated imidazole ligand is useful to develop emission and redox switching materials by protonation. Taking advantage of molecular designs based on both redox-active and proton-responsive behavior, further work will pave the road towards the design and development of diverse molecular-based functional materials with stimuli response.

Supplementary Materials: The following are available online at https://www.mdpi.com/article/10.3390/inorganics9040024/s1, X-Ray crystallographic data for complex **1**; the CIF and the checkCIF output files are included in the Supplementary Materials. Figure S1. ^{1}H and ^{13}C NMR spectra of **1** in CD_3CN-d_3. Figure S2. IR spectra of HL (green) and complex **1** (red). Figure S3. UV-Vis absorption spectra of HL and L^- in DMF (left) and cyclic voltammograms of HL and L^- in CH_2Cl_2 (left). Figure S4. Calculated frontier orbitals for the optical transitions observed in 1. Orbitals are shown with an iso-value of 0.06. Figure S5 Calculated frontier orbitals for the optical transitions observed in H^+-1. Orbitals are shown with an iso-value of 0.06. Figure S6 UV-Vis absorption spectral changes of complex 1 with Et_3N after addition of 1.6 eq. TfOH. Figure S7 Cyclic voltammograms of complex 1 in acetonitrile before and after the addition of 1.6 eq. of TfOH. Table S1. Main TD-DFT calculated transition of 1 compared with experimental data. Table S2. Main TD-DFT calculated transition of H^+-1 compared with experimental data. Table S3. Cartesian coordinates of geometry optimized 1. Table S4 Cartesian coordinates of geometry optimized H^+-1.

Author Contributions: Formal analysis, M.T.; data curation, M.T.; writing—original draft preparation, T.S.; writing—review and editing, M.N. and H.O. All authors have read and agreed to the published version of the manuscript.

Institutional Review Board Statement: Not applicable.

Informed Consent Statement: Not applicable.

Data Availability Statement: Not applicable.

Conflicts of Interest: The authors declare no conflict of interest.

References

1. Cai, W.; Wang, J.; Chu, C.; Chen, W.; Wu, C.; Liu, G. Metal-Organic Framework-Based Stimuli-Responsive Systems for Drug Delivery. *Adv. Sci.* **2019**, *6*, 1801526. [CrossRef]
2. Baroncini, M.; Silvi, S.; Credi, A. Photo- and Redox-Driven Artificial Molecular Motors. *Chem. Rev.* **2020**, *120*, 200–268. [CrossRef] [PubMed]

3. McConnell, A.J.; Wood, C.S.; Neelakandan, P.P.; Nitschke, J.R. Stimuli-Responsive Metal-Ligand Assemblies. *Chem. Rev.* **2015**, *115*, 7729–7793. [CrossRef]

4. Li, Z.; Yin, Y. Stimuli-Responsive Optical Nanomaterials. *Adv. Mater.* **2019**, *31*, 1807061. [CrossRef]

5. Kurihara, M.; Nishihara, H. Azo- and Quinone-conjugated Redox Complexes Photo- and Proton-coupled Intramolecular Reactions Based on d-π Interaction. *Coord. Chem. Rev.* **2002**, *226*, 125–135. [CrossRef]

6. Mako, T.L.; Racicot, J.M.; Levine, M. Supramolecular Luminescent Sensors. *Chem. Rev.* **2019**, *119*, 322–477. [CrossRef]

7. Kumar, R.; Sharma, A.; Singh, H.; Suating, P.; Kim, H.S.; Sunwoo, K.; Shim, I.; Gibb, B.C.; Kim, J.S. Revisiting Fluorescent Calixarenes: From Molecular Sensor to Smart Materials. *Chem. Rev.* **2019**, *119*, 9657–9721. [CrossRef]

8. Murray, J.; Kim, K.; Ogoshi, T.; Yao, W.; Gibb, B.C. The Aqueous Supramolecular Chemistry of Cucurbit[n]urils, Pillar[n]arenes and deep-cavity Cavitands. *Chem. Soc. Rev.* **2017**, *46*, 2479–2496. [CrossRef] [PubMed]

9. Martinez-Manez, R.; Sancenon, F. Fluorogenic and Chromogenic Chemosensors and Reagents for Anions. *Chem. Rev.* **2003**, *103*, 4419–4476. [CrossRef]

10. Silva, A.P.; Gunaratne, H.Q.N.; Gunnlaugsson, T.; Huxley, A.J.M.; McCoy, C.P.; Rademacher, J.T.; Rice, T.E. Signaling Recognition Events with Fluorescent Sensors and Switches. *Chem. Rev.* **1997**, *97*, 1515–1566. [CrossRef] [PubMed]

11. Gao, F.; Chen, X.; Zhou, F.; Weng, L.-P.; Guo, L.-T.; Chen, M.; Chao, H.; Ji, L.-N. pH Responsive Luminescent Switches of Ruthenium(II) Complexes Containing Two Imidazole Groups: Synthesis, Spectroscopy, Electrochemistry and Theoretical Calculations. *Inorg. Chim. Acta* **2009**, *362*, 4960–4966. [CrossRef]

12. Ahn, H.; Hong, J.; Kim, S.Y.; Choi, I.; Park, M.J. A pH-Responsive Molecular Switch with Tricolor Luminescence. *ACS Appl. Mater. Interfaces* **2015**, *7*, 704–712. [CrossRef] [PubMed]

13. Kobayashi, K.; Ohtsu, H.; Wada, T.; Kato, T.; Tanaka, K. Characterization of a Stable Ruthenium Complex with an Oxyl Radical. *J. Am. Chem. Soc.* **2003**, *125*, 6729–6739. [CrossRef]

14. Kojima, T.; Hayashi, K.; Matsuda, Y. Structures and Properties of Ruthenium(II) Complexes of Pyridylamine Ligands with Oxygen-Bound Amide Moieties: Regulation of Structures and Proton-Coupled Electron Transfer. *Inorg. Chem.* **2004**, *43*, 6793–6804. [CrossRef]

15. Di Pietro, C.; Serroni, S.; Campagna, S.; Gandolfi, M.T.; Ballardini, R.; Fanni, S.; Browne, W.R.; Vos, J.G. Proton Controlled Intramolecular Communication in Dinuclear Ruthenium(II) Polypyridine Complexes. *Inorg. Chem.* **2002**, *41*, 2871–2878. [CrossRef]

16. Haga, M.; Ano, T.; Kano, K.; Yamabe, S. Proton-induced Switching of Metal-metal Interactions in Dinuclear Ruthenium and Osmium Complexes Bridged by 2,2′-Bis(2-pyridyl)bibenzimidazole. *Inorg. Chem.* **1991**, *30*, 3843–3849. [CrossRef]

17. Huynh, M.H.V.; Meyer, T.J. Proton-Coupled Electron Transfer. *Chem. Rev.* **2007**, *107*, 5004–5064. [CrossRef]

18. Weinberg, D.R.; Gagliardi, C.J.; Hull, J.F.; Murphy, C.F.; Kent, C.A.; Westlake, B.C.; Paul, A.; Ess, D.H.; McCafferty, D.G.; Meyer, T.J. Proton-Coupled Electron Transfer. *Chem. Rev.* **2012**, *112*, 4016–4093. [CrossRef]

19. Zhang, J.; Chen, J.; Xu, B.; Wang, L.; Ma, S.; Dong, Y.; Li, B.; Ye, L.; Tian, W. Remarkable Fluorescence Change Based on the Protonation-deprotonation Control in Organic Crystals. *Chem. Commun.* **2013**, *49*, 3878–3880. [CrossRef]

20. Sato, O. Dynamic Molecular Crystals with Switchable Physical Properties. *Nat. Chem.* **2016**, *8*, 644–656. [CrossRef]

21. Gütlich, P.; Gaspar, A.B.; Garcia, Y. Spin State Switching in Iron Coordination Compounds. *Beilstein J. Org. Chem.* **2013**, *9*, 342–391. [CrossRef]

22. Nihei, M. Molecular Prussian Blue Analogues: From Bulk to Molecules and Low-dimensional Aggregates. *Chem. Lett.* **2020**, *49*, 1206–1215. [CrossRef]

23. Nihei, M.; Yanai, Y.; Hsu, I.-J.; Sekine, Y.; Oshio, H. A Hydrogen-Bonded Cyanide-Bridged [Co$_2$Fe$_2$] Square Complex Exhibiting a Three-Step Spin Transition. *Angew. Chem. Int. Ed.* **2017**, *56*, 591–594. [CrossRef] [PubMed]

24. Sekine, Y.; Nihei, M.; Oshio, H. Dimensionally controlled assembly of an external stimuli-responsive [Co$_2$Fe$_2$] complex into supramolecular hydrogen-bonded networks. *Chem. Eur. J.* **2017**, *23*, 5193–5197. [CrossRef] [PubMed]

25. Luo, Y.-H.; Nihei, M.; Wen, G.-J.; Sun, B.-W.; Oshio, H. Ambient-Temperature Spin-State Switching Achieved by Protonation of the Amino Group in [Fe(H$_2$Bpz$_2$)$_2$(bipy-NH$_2$)]. *Inorg. Chem.* **2016**, *55*, 8147–8152. [CrossRef] [PubMed]

26. Shiga, T.; Saiki, R.; Akiyama, L.; Kumai, R.; Natke, D.; Renz, F.; Cameron, J.; Newton, G.N.; Oshio, H. A Brønsted ligand molecular switch with five accessible states. *Angew. Chem. Int. Ed.* **2019**, *58*, 5658–5662. [CrossRef]

27. Takumi Nakanishi, T.; Hori, Y.; Sato, H.; Wu, S.Q.; Okazawa, A.; Kojima, N.; Yamamoto, T.; Einaga, Y.; Hayami, S.; Horie, Y.; et al. Observation of Proton Transfer Coupled Spin Transition and Trapping of Photoinduced Metastable Proton Transfer State in an Fe(II) Complex. *J. Am. Chem. Soc.* **2019**, *141*, 14384–14393. [CrossRef]

28. Ueda, A.; Yamada, S.; Isono, T.; Kamo, H.; Nakao, A.; Kumai, R.; Nakao, H.; Murakami, Y.; Yamamoto, K.; Nishio, Y.; et al. Hydrogen-Bond-Dynamics-Based Switching of Conductivity and Magnetism: A Phase Transition Caused by Deuterium and Electron Transfer in a Hydrogen-Bonded Purely Organic Conductor Crystal. *J. Am. Chem. Soc.* **2014**, *136*, 12184–12192. [CrossRef]

29. Shiga, T.; Kumamaru, R.; Newton, G.N.; Oshio, H. Heteroleptic Iron(II) Complexes with Naphthoquinone-type Ligands. *Dalton Trans.* **2020**, *49*, 1485–1491. [CrossRef]

30. Bar, M.; Deb, S.; Paul, A.; Baitalik, S. Stimuli-Responsive Luminescent Bis-Tridentate Ru(II) Complexes toward the Design of Functional Materials. *Inorg. Chem.* **2018**, *57*, 12010–12024. [CrossRef]

31. Pal, P.; Ganguly, T.; Dasa, S.; Baitalik, S. pH-Responsive colorimetric, emission and redox switches based on Ru(II)-terpyridine complexes. *Dalton Trans.* **2021**. [CrossRef]

32. Duan, L.; Moyses, C.A.; Ahlquist, M.S.G.; Sun, L. Highly Efficient and Robust Molecular Ruthenium Catalysts for Water Oxidation. *Proc. Natl. Acad. Sci. USA* **2012**, *109*, 15584–15588. [CrossRef]
33. Fujita, E. Photochemical Carbon Dioxide Reduction with Metal Complexes. *Coord. Chem. Rev.* **1999**, *185–186*, 373–384. [CrossRef]
34. Mede, T.; Jäger, M.; Schubert, U.S. High-Yielding Syntheses of Multifunctionalized Ru^{II} Polypyridyl-Type Sensitizer: Experimental and Computatinal Insight into Coordination. *Inorg. Chem.* **2019**, *58*, 9822–9832. [CrossRef]
35. Jiang, C.-W.; Chao, H.; Li, H.; Ji, L.-N. Syntheses, Characterization and DNA-binding Studies of Ruthenium(II) Terpyridine Complexes: [Ru(tpy)(PHBI)]$^{2+}$ and [Ru(tpy)(PHNI)]$^{2+}$. *J. Inorg. Bio.* **2003**, *93*, 247–255. [CrossRef]
36. Zhang, G.; Zong, R.; Tseng, H.-W.; Thummel, R.P. Ru(II) Complexes of Tetradentate Ligands Related to 2,9-Di(pyrid-2′-yl)-1,10-phenanthroline. *Inorg. Chem.* **2008**, *47*, 990–998. [CrossRef] [PubMed]
37. Liu, Y.-J.; Chao, H.; Tan, L.-F.; Yuan, Y.-X.; Wei, W.; Ji, L.-N. Interaction of Polypyridyl Ruthenium(II) Complex Containing Asymmetric Ligand with DNA. *J. Inorg. Biol.* **2005**, *99*, 530–537. [CrossRef]
38. Mardanya, S.; Mondal, D.; Baitalik, S. Biometallic Ru(II) and Os(II) Complexes Based on a Pyrene-bisimidazole spacer: Synthesis, Photophysics, Electrochemistry and Multisignalling DNA Binding Studies in the Near Infrared Region. *Dalton Trans.* **2017**, *46*, 17010–17024. [CrossRef] [PubMed]
39. Haga, M. Synthesis and Protonation-deprotonation Reactions of Ruthesium(II) Complexes Containing 2,2′-Bibenzimidazole and Reelated Ligands. *Inorg. Chim. Acta* **1983**, *75*, 29–35. [CrossRef]
40. Sorsche, D.; Rommel, S.A.; Rau, S. Functional Dimming of Pincer-Shaped Bibenziimidazole-Ruthenium(II) Complexes with Improved Anion-Sensitive Luminescence. *Eur. J. Inorg. Chem.* **2016**, *2016*, 1503–1513. [CrossRef]
41. Parthiban, C.; Ciattini, S.; Chalazziand, L.; Elango, K.P. Colorimetric sensing of anions by Cu(II), Co(II), Ni(II) and Zn(II) complexes of naphthoquinone-imidazole hybrid-Influence of complex formation on selectivity and sensing medium. *Sens. Actuators B* **2016**, *231*, 768–778. [CrossRef]
42. Balzani, A.J.V.; Barigelletti, F.; Campagna, S.; Belser, P.; Zelewsky, A. Ru(II) Polypyridine Complexes: Photophysics, Photochemistry, Eletrochemistry, and Chemiluminescence. *Coord. Chem. Rev.* **1988**, *84*, 85–277.
43. Hohloch, S.; Schweinfurth, D.; Sommer, M.G.; Weisser, F.; Deibel, N.; Ehret, F.; Sarkar, B. The Redox Series [Ru(bpy)$_2$(L)]$_n$, *n* = +3, +2, +1, 0, with L = Bipyridine, "Click" Derived Pyridyl-triazole or Bis-triazole: A Combined Structural, Electrochemical, Spectroelectrochemical and DFT investigation. *Dalton Trans.* **2014**, *43*, 4437–4450. [CrossRef]
44. Sullivan, B.P.; Salmon, T.J.; Meyer, T.J. Mixed Phosphine 2,2′-Bipyridine Complexes of Ruthenium. *Inorg. Chem.* **1978**, *17*, 3334–3341. [CrossRef]
45. Chen, J.; Jin, B. Investigation on Redox Mechanism of 1,4-Naphthoquinone by in situ FT-IR Spectroelectrochemistry. *J. Electro. Chem.* **2015**, *756*, 36–42. [CrossRef]
46. Manivannan, R.; Satheshkumar, A.; Elango, K.P. Tuning of the H-bonding Ability of Imidazole N-H Towards the Colorimetric Sensing of Fluoride and Cyanide Ions as Their Sodium Salts in Water. *New J. Chem.* **2013**, *37*, 3152–3160. [CrossRef]
47. Pan, L.; Zheng, Q.; Chen, Y.; Yang, R.; Yang, Y.; Li, Z.; Meng, X. Design, Synthesis and Biological Evaluation of Novel Naphthoquinone Derivatives as IDO1 Inhibitors. *Eur. J. Med. Chem.* **2018**, *157*, 423–436. [CrossRef]
48. Liu, Z.; Zhang, Z.; Zhang, W.; Yan, D. 2-Substituted-1-(2-morpholinoethyl)-1H-naphtho[2,3-d]imidazole-4,9-diones: Design, Synthesis and Antiproliferative Activity. *Bioorg. Med. Chem. Lett.* **2018**, *28*, 2454–2458. [CrossRef] [PubMed]
49. Sheldrick, G.M. *SHELXL-2013. Program for the Refinement of Crystal Structures*; University of Göttingen: Göttingen, Germany, 2013.
50. Sheldrick, G.M. *SADABS*; University of Göttingen: Göttingen, Germany, 1996.
51. Becke, A.D. Density-Functional Thermochemistry. III. The Role of Exact Exchange. *J. Chem. Phys.* **1993**, *98*, 5648–5652. [CrossRef]
52. Frisch, M.J.; Trucks, G.W.; Schlegel, H.B.; Scuseria, G.E.; Robb, M.A.; Cheeseman, J.R.; Scalmani, G.; Barone, V.; Petersson, G.A.; Nakatsuji, H.; et al. *Gaussian 16, Revision A.03*; Gaussian Inc.: Wallingford, CT, USA, 2010.
53. Hay, P.J.; Wadt, W.R. Ab Initio Effective Core Potentials for Molecular Calculations. Potentials for K and Au Including the Outermost Core Orbitals. *J. Chem. Phys.* **1985**, *82*, 299–310. [CrossRef]
54. Hay, P.J.; Wadt, W.R. Ab Initio Effective Core Potentials for Molecular Calculations. Potentials for the Transition Metal Atoms Sc to Hg. *J. Chem. Phys.* **1985**, *82*, 270–283. [CrossRef]
55. Wadt, W.R.; Hay, P.J. Ab Initio Effective Core Potentials for Molecular Calculations. Potentials for Main Group Elements Na to Bi. *J. Chem. Phys.* **1985**, *82*, 284–298. [CrossRef]
56. Barone, V.; Cossi, M. Quantum Calculation of Molecular Energies and Energy Gradients in Solution by a Conductor Solvent Model. *J. Phys. Chem. A* **1998**, *102*, 1995–2001. [CrossRef]